NJC

PAPER

View Article Online
View Journal

Cite this: DOI: 10.1039/d5nj03611a

Fabrication of manganese-loaded lignin-derived carbon *via* an *in situ* anchoring strategy for water electrolysis

Yang Huamei,[ab] Wang Beilei,[a] Yu Mengjun,[a] He Haiyan[bc] and Li Changzhi *[bc]

Low-cost, high-performance catalysts are pivotal for advancing water electrolysis toward industrial applications. As an abundant, renewable, and readily available carbon feedstock, lignin offers a sustainable platform for the development of a carbon-supported catalyst. In this study, manganese-loaded lignin-derived carbon (Mn_x@C) was synthesized *via* an *in situ* chelation–anchoring strategy using lignin as the carbon source. The *in situ* chelation–anchoring carbonization process enabled effective incorporation and uniform dispersion of Mn species. Mn species in Mn_x@C were mainly Mn_2O_3, MnO_2, and MnO. Among these Mn species, MnO was dispersed in the lignin-based carbon support as aggregation nanoparticles, while Mn_2O_3 and MnO_2 were primarily dispersed in an amorphous state. The electrocatalytic performances of Mn_x@C were systematically evaluated for the oxygen evolution reaction (OER) and hydrogen evolution reaction (HER). The Mn content and NH_4Cl modification significantly influenced the OER and HER activities. The Mn_1@C prepared at 1 mmol Mn/g lignin, with the final Mn content of 8.7%, exhibited optimal performances of 517 mV (OER) and 448 mV (HER) at 50 mA cm^{-2}. Further improvement was achieved by modulating the pore structure using NH_4Cl as a pore-forming agent, resulting in a Mn-loaded and nitrogen-doped carbon (Mn_1@NC). NH_4Cl modification induced a morphological transition from a bulk structure to a layered microporous structure with a high surface area. The modified Mn_1@NC demonstrated excellent OER and HER performances, requiring low overpotentials of 299 mV (OER) and 409 mV (HER) at 50 mA cm^{-2}. In addition, the overall water-splitting demonstrated a low potential of 1.65 V to reach 10 mA cm^{-2}. This *in situ* anchoring and direct carbonization strategy provides a simple, cost-effective, and scalable route to high-performance Mn-based catalysts from low-cost lignin, offering potential for industrial water electrolysis and high-efficient utilization of lignin.

Received 9th September 2025,
Accepted 19th November 2025

DOI: 10.1039/d5nj03611a

rsc.li/njc

Introduction

Water electrolysis is a promising sustainable technology for hydrogen production with significant application potential.[1,2] Catalysts play a pivotal role in reducing the kinetic barriers associated with the oxygen evolution reaction (OER) and hydrogen evolution reaction (HER) during water electrolysis. State-of-the-art catalysts rely heavily on scarce precious metals (such as Pt, Ru and Ir compounds),[3–7] leading to prohibitively high costs that impede large-scale applications. Consequently, developing non-precious metal catalysts with high activity for water electrolysis is imperative as alternatives to precious metal-based catalysts.[8,9]

Transition metals and their oxides, nitrides, phosphides, hydroxides and sulfides have been widely investigated.[7,8,10–13] Manganese (Mn), a typical 3d transition metal, is derived primarily from parent materials in soil, and exhibits multiple oxidation states. Mn-based materials have been explored as electrocatalysts for the OER and HER owing to their inherent catalytic activity, environmental compatibility, low cost, and natural abundance.[14–19] Particularly, Mn-based oxides (MnO_x) exhibit good chemical stability in alkaline electrolytes[20,21] and facilitate O–O bond formation steps in the OER owing to its variable oxidation states (commonly +2 in MnO, +3 in Mn_2O_3, +4 in MnO_2, and mixed states in Mn_3O_4).[20] Therefore, focused development of Mn-based catalysts remains necessary, as they possess irreplaceable potential in large-scale commercial applications. However, Mn-based materials always exhibit poor OER and HER performances compared to other transition metal-based materials (such as iron, nickel, and cobalt-based materials), limiting their practical applications.[7,12,21,22] The lower electrocatalytic activity of Mn-based catalysts, leading to low

[a] School of Materials and Chemical Engineering, Xuzhou University of Technology, Xuzhou, Jiangsu, 221018, China
[b] CAS Key Laboratory of Science and Technology on Applied Catalysis, Dalian Institute of Chemical Physics, Chinese Academy of Sciences, Dalian, 116023, China. E-mail: licz@dicp.ac.cn
[c] University of Chinese Academy of Sciences, Beijing 100049, China

intrinsic catalytic activity,[3,8,12,23] is primarily caused by the poor electrical conductivity and the electronic configuration that results in weak electronic coupling with intermediates.[20,21]

The performance of Mn-based catalysts can be improved through the following strategies: constructing heterostructures (*e.g.*, composites with carbon materials or oxides) to increase the number of active sites and enhance the electron transfer rate and charge transfer efficiency. Regulating the morphology (*e.g.*, preparing nanosheets or hollow spheres) to increase specific surface area exposes more active sites for the OER and the HER. Carbon-based materials are employed as electrically active materials or conductive substrates to create oxygen vacancies and heterogeneous interfaces. The OER and HER performance of MnO_x-based electrocatalysts can be improved by tuning the morphology of carbon materials and synergistic effects between Mn species and carbon.[18,19,24–26] Carbon supports such as activated carbon, carbon nanotubes, graphene, and carbon nanofibers are always employed to prepare Mn-loading carbon catalysts *via* an impregnation method. However, these carbon supports need to be prepared in advance, making the process labor- and time-intensive. Meanwhile, these carbon supports often possess inert surfaces that limit metal dispersion during impregnation.[27] Recently, well-synthetic carbon materials such as carbon dots[18,28] and metal–organic frameworks[29,30] were employed to incorporate with Mn species. This strategy can provide Mn-based carbon catalysts with high surface areas, enhanced conductivity, greatly promoted electrocatalytic activity and high stability for the OER. However, the reliance on pure chemicals as carbon precursors incurs high costs, hindering large-scale application.

Lignin, a renewable biomass resource, possesses a highly aromatic, three-dimensional conjugated network with abundant oxygen-containing functional groups (*e.g.*, hydroxyl, carbonyl, and methoxy) and high carbon content.[31] These structural characteristics endow lignin with compelling potential for synthesizing multifunctional carbon materials, particularly in applications such as energy storage, adsorption, and catalysis.[31–37] Notably, the oxygen functional groups can effectively anchor metal species through chelation or coordination, promoting uniform metal dispersion and enhancing catalytic performance.[36] Owing to these advantages, lignin is regarded as an ideal precursor for designing high-performance functional carbon supports in catalytic applications. At the same time, lignin is a large-volume by-product of the pulping and papermaking as well as biorefinery industries. Lignin is a large-volume byproduct of the pulping and papermaking as well as biorefinery industries. It exhibits a substantial annual production volume, yet the majority is currently underutilized through low-value applications such as disposal or inefficient combustion, which pose environmental and economic challenges. Using it as a carbon source can achieve ''waste resource utilization'' and reduce the preparation cost of carbon materials.

In this work, a Mn-loaded lignin-derived carbon catalyst (Mn_x@C) was prepared for water electrolysis *via* an *in situ* anchoring and one-step carbonization strategy. The effect of Mn proportion was investigated, and Mn_1@C obtained at the Mn proportion of 1 mmol g^{-1} lignin exhibited the best OER and HER performances. Furthermore, morphological modulation using ammonium chloride (NH_4Cl) as a pore-forming agent yielded Mn_1@NC with a porous lamellar structure, characterized by high surface area and abundant micropores. This optimized structure significantly enhanced bifunctional OER and HER performances. The Mn_1@NC catalyst exhibited a remarkably low overpotential of 299 mV for the OER and 409 mV for the HER at a current density of 50 mA cm^{-2}. In addition, the overall water-splitting device demonstrated a low potential of 1.65 V to reach 10 mA cm^{-2}. This performance conclusively demonstrates the viability of fabricating high-performance bifunctional electrocatalysts for water electrolysis through the *in situ* chelation and carbonization methodology utilizing lignin as a carbon precursor.

Experimental

Experimental instruments and reagents

Lignin, purchased from Shandong Longli Biotechnology Co., Ltd, 200 mesh, vacuum-dried at 80 °C for 12 hours. Polyvinylpyrrolidone (PVP), Shanghai Titan Technology Co., Ltd, RG; carbon black, Shanghai Titan Technology Co., Ltd, RG; anhydrous ethanol, Shanghai Titan Technology Co., Ltd, ≥99.7%; ammonium chloride (NH_4Cl), Shanghai Titan Technology Co., Ltd, ≥99.5%; manganese(II) tetrahydrate chloride ($MnCl_2 \cdot 4H_2O$), Shanghai Titan Technology Co., Ltd, ≥99%.

Preparation of Mn_x@C and Mn_x@NC

Mn_x@C was prepared *via* an *in situ* anchoring and one-step carbonization strategy. The specific process was as follows: lignin molecules first combined with Mn ions to form a stable manganese–lignin complex (Mn–lignin) *via* coordinate bonds, and then the complex underwent high-temperature carbonization under an inert atmosphere to obtain Mn_x@C. Typically, 1 g of lignin was added to 10 mL of ethanol and ultrasonicated for 15 minutes to achieve complete dispersion, forming a suspension. 0.198 g (1 mmol) of $MnCl_2 \cdot 4H_2O$ was dissolved in 10 mL of ethanol/water (V : V 2 : 1). Under ultrasonication, the $MnCl_2$ solution was added dropwise using a pipette to the lignin–ethanol suspension, forming a mixture. This mixture was then magnetically stirred for 24 hours. Subsequently, 50 mL of deionized water was added to the ethanol suspension of Mn–lignin, and the suspension was left to stand for 30 minutes. Mn–lignin complex precipitated out and settled. Vacuum filtration was performed to obtain the Mn–lignin complex. The Mn–lignin complex was dried in a vacuum oven at 80 °C for 10 hours. The dried Mn–lignin sample was placed in a porcelain boat and transferred to a tubular furnace for high-temperature carbonization. The heating program, under a nitrogen atmosphere, was as follows: ramp the temperature at 15 °C min^{-1} to 800 °C and then hold at 800 °C for 2 hours. After carbonization, the furnace was cooled naturally to room temperature under nitrogen, and Mn-loaded lignin carbon-based materials were obtained, which were labelled as Mn_x@C (x was the millimole ratio of $MnCl_2 \cdot 4H_2O$ to lignin). For example, samples prepared with 0.198 g (1 mmol) of $MnCl_2 \cdot 4H_2O$ added to 1 g lignin were labelled as Mn_1@C. The effect of Mn loading

was investigated with the Mn proportion x being 0 (0 g), 0.05 (0.010 g of $MnCl_2{\cdot}4H_2O$, 0.05 mmol), 0.25 (0.049 g of $MnCl_2{\cdot}4H_2O$, 0.25 mmol), 0.5 (0.099 g of $MnCl_2{\cdot}4H_2O$, 0.5 mmol), 1 (0.198 g of $MnCl_2{\cdot}4H_2O$, 1 mmol), and 2 (0.396 g of $MnCl_2{\cdot}4H_2O$, 2 mmol).

Additionally, NH_4Cl was employed to modify the catalytic performance of Mn_1@C, which served as a pore-forming agent and a nitrogen source. The preparation of the Mn–lignin complex followed the same procedure as Mn_1@C. Wetting grinding was employed to achieve thorough mixing of Mn–lignin and NH_4Cl with the ratio of NH_4Cl to lignin as 0.5 : 1. 0.5 g NH_4Cl was added to the complex of Mn–lignin, and the mixture was subjected to wetting grinding for complete homogenization. The mixture of Mn–lignin and NH_4Cl was dried in a vacuum oven at 80 °C for 12 hours. Finally, the mixture of Mn–lignin and NH_4Cl was carbonized *via* the same procedure of Mn_1@C. The modified N-doped carbon was labelled as Mn_1@NC. An N-doped lignin-based carbon without Mn-loading (Mn_0@NC) was also prepared using the same procedure as Mn_1@NC.

For control experiments, activated carbon (AC) was employed to prepare a Mn-loaded activated carbon (Mn_1@AC) with 0.198 g of $MnCl_2{\cdot}4H_2O$, using the same method as Mn_1@C.

Electrochemical testing

Nickel foam was cut into 1.2 × 1 cm^2 squares. The nickel foam squares were cleaned by sequential immersion in 3 mol L^{-1} hydrochloric acid, acetone, deionized water, and ethanol, vacuum-dried at 60 °C for 12 hours. The high-temperature carbonized samples were weighed according to the mass ratio (8 : 1 : 1) of carbon black, PVP and samples. Typically, 0.08 g of carbon black, 0.01 g of PVP and 0.01 g of samples were weighed and mixed. The mixture was ground with 2 ml of ethanol to form a homogeneous slurry. The nickel foam was immersed in the above slurry for 1 minute and rapidly dried using a heat lamp. The nickel foam was weighed before and after loading catalytic materials by a microbalance. The average loaded mass was 0.8 ± 0.05 mg cm^{-2}. Then, the loaded foam nickel was placed in a vacuum oven at 60 °C for 12 hours.

All electrochemical OER and HER tests were performed on a CHI660E electrochemical workstation using a standard three-electrode system in 1 M KOH electrolyte (pH = 14) at room temperature. The fabricated nickel foam electrode (clamped with an electrode holder) was used as the working electrode, and the area of the working electrode immersed in the KOH solution was kept as 1 × 1 cm^2. The platinum sheet was used as the counter electrode. The mercury/mercury oxide (Hg/HgO) electrode (1 M KOH, 25 °C, standard potential +0.098 V *vs.* SHE) was used as the reference electrode.

Linear sweep voltammetry (LSV) for the OER was performed in the potential range of 0 to 1 V *vs.* Hg/HgO. All measured potentials (*vs.* Hg/HgO) were converted to the reversible hydrogen electrode (RHE) scale using the formula under alkaline conditions: V (*vs.* RHE) = V (*vs.* Hg/HgO) +0.098 + 0.059 × pH. Tafel slopes (b) were calculated by fitting the linear region of the Tafel plot using the equation: $\eta = a + b\log j$, where η is the overpotential ($\eta = E - E_{rev}$, E_{rev} = 1.23 V), a is a constant, and j is the current density. Cyclic voltammetry (CV) was performed within the non-faradaic potential range (typically 0.1 to 0.2 V *vs.* RHE is recommended; confirm suitability for your system) at various scan rates (*e.g.*, 10, 40, 80, and 100 mV s^{-1}). The double-layer capacitance (C_{dl}) was estimated from the slope of the plot of the charging current density difference ($\Delta j = |j_a - j_c|/2$) at a fixed potential within this range *versus* the scan rate. The long-term electrochemical stability of the catalyst was evaluated by chronopotentiometry or chronoamperometry at a constant current density or potential in 1 M KOH (pH = 14) for 20 hours. Electrochemical impedance spectroscopy (EIS) was conducted from a potential of 238 to 458 mV *vs.* RHE for the OER over a frequency range from 100 kHz to 0.1 Hz with an AC amplitude of 10 mV. LSV measurements for the HER were performed in the potential range of −0.9 to 0.0 V *vs.* Hg/HgO. LSV measurements for the overall water-splitting were conducted using a two-electrode system in 1.0 M KOH solution, with Mn_1@NC serving as both the cathode and the anode (Mn_1@NC‖Mn_1@NC).

Characterization

The Mn contents in Mn_x@C, Mn_1@AC and Mn_1@NC were determined by ICP-OES. The contents of carbon (C), hydrogen (H) and nitrogen (N) in lignin, Mn_x@C, Mn_1@AC and Mn_1@NC were determined by using an elemental analyzer. Powder X-ray diffraction patterns were collected using a multi-purpose X-ray diffractometer with Cu Kα radiation (λ = 1.5418 Å). Samples were prepared by pressing the catalyst powder onto a sample holder, cleaning the surface with anhydrous ethanol, and drying. Measurements were performed with a tube voltage of 40 kV, a tube current of 40 mA, a scan rate of 2° min^{-1}, and a scan range of 5° to 90° (2θ). The textural properties (specific surface area, pore volume, and pore size distribution) of the samples were determined by N_2 adsorption–desorption isotherms measured at −196 °C. Specific surface area was calculated using the Brunauer–Emmett–Teller (BET) method. Pore size distribution was analyzed using density functional theory (DFT) or non-local density functional theory (NLDFT) methods for micropores (<2 nm) and mesopores. The morphology of the samples was characterized at different scales using scanning electron microscopy (SEM) and transmission electron microscopy (TEM) with energy-dispersive X-ray spectroscopy (EDS).

Results and discussion

Structural characterization

Table 1 shows that Mn content in Mn_x@C increased to 9.74 wt% with the Mn proportion increasing to 2 mmol g^{-1}. Lignin employed in this work was mainly composed of 63.3 wt% carbon (C), 5.9 wt% hydrogen (H), 28.9 wt% oxygen (O), and 1.9 wt% nitrogen (N), as listed in Table 1. Without the addition of Mn and NH_4Cl, the carbon yield from lignin, labelled as Mn_0@C, was 35.6%. The content of C, H, O and N was 83.82%, 2.67%, 13.06% and 0.43%, respectively. Mn_x@C, prepared through an *in situ* anchoring and one-step carbonization strategy, had a higher content of C than lignin, and a lower content of H, N and O.

Table 1 Elemental composition of Mn_x@C and the intensity ratio of $I_{40.5}/I_{22.4}$ calculated based on XRD

Samples	Mn[a]/%	C[b]/%	H[c]/%	N[d]/%	O[e]/%	$I_{40.5}/I_{22.4}$[f]
Lignin	—	63.32	5.91	1.87	28.90	—
Mn_0@C	0.02	83.82	2.67	0.43	13.06	—
$Mn_{0.05}$@C	0.55	83.71	2.21	0.42	13.11	0.98
$Mn_{0.25}$@C	2.87	80.54	2.73	0.51	13.35	1.42
$Mn_{0.5}$@C	5.84	78.63	1.32	0.74	13.47	4.65
Mn_1@C	8.65	75.48	1.45	0.82	13.60	5.28
Mn_2@C	9.74	72.22	0.94	0.85	16.25	3.74
Mn_1@AC	6.63	87.37	1.42	0.38	4.20	—
Mn_1@NC	8.92	72.23	2.13	4.36	12.36	5.22

[a] Determined by ICP-OES. [b] Determined by using an elemental analyzer. [c] Determined by using an elemental analyzer. [d] Determined by using an elemental analyzer. [e] Determined by the difference of 100 and the sum of a–d. [f] $I_{40.5}/I_C$ calculated based on XRD, as shown in Fig. 1.

With the increase in Mn content, the C content decreased while the contents of N and O increased, suggesting that the introduced Mn immobilized O and N. Activated carbon (AC) was employed to prepare a Mn-loaded catalyst (Mn_1@AC) with the Mn proportion of 1 mmol g^{-1} AC. Table 1 shows that Mn_1@AC had a higher C content and a much lower O content than Mn_1@C. The Mn content in Mn_1@AC was 6.63 wt%, slightly lower than Mn_1@C.

The addition of NH_4Cl during the carbonization process achieved N-doped carbon (Mn_1@NC) with the Mn proportion of 1 mmol g^{-1} lignin, which had a much higher N content than Mn_1@C and Mn_1@AC as listed in Table 1. As mentioned above, lignin has abundant active functional groups in its structure, including hydroxyl, carbonyl, and carboxyl groups. Meanwhile, lignin was decomposed to form active carbon intermediates during carbonization.[38] The co-carbonization of NH_4Cl and the Mn–lignin complex achieved nitrogen doping and morphology regulation through a synergistic effect due to the abundant active structures in lignin.[39] At around 280 °C, NH_4Cl decomposed to generate gases (NH_3 and HCl). NH_3 reacted with these carbon intermediates or active groups, and N was embedded into the carbon skeleton through substitution, cyclization, and other reactions, realizing *in situ* N-doping.[38–40] As the carbon skeleton further graphitized, nitrogen stably existed in the carbon structure (mainly in three forms: pyrrole nitrogen, pyridine nitrogen, and graphitic nitrogen). The EDS and XPS analysis results in the following section will confirm the N-doping and its existing forms.

Fig. 1(a) shows the XRD patterns of Mn_x@C, Mn_1@AC and Mn_1@NC. Mn_0@C, derived from lignin carbonization without Mn-loading, was composed of an amorphous carbon structure with a diffraction peak at 2θ = 22.4°. With the increasing Mn proportion, the diffraction peaks at 2θ = 35.6°, 40.5°, 59.1°, 70.1°, and 73.6° intensified. These peaks corresponded to the diffraction peaks of the MnO standard card (PDF#89-2804), indicating that Mn was successfully loaded onto the carbon support and existed in the form of MnO. Taking the intensity of the carbon peak (2θ = 22.4°, $I_{22.4}$) as a reference, the intensity ratio of the MnO characteristic peak ($I_{40.5}$) to $I_{22.4}$ ($I_{40.5}/I_{22.4}$) was calculated to semi-quantitatively analyze the loading amount of MnO as listed in Table 1. The loading amount of MnO increased with the increasing Mn proportion, which was consistent with the results of ICP-OES. The loading amount of MnO in Mn_1@C reached the maximum with the peak value of $I_{40.5}/I_{22.4}$ as listed in Table 1. When NH_4Cl was added for pore generation, the XRD pattern of Mn_1@NC had no significant changes, indicating that the addition of NH_4Cl had no effects on Mn species. However, Mn_1@AC had no distinct diffraction peaks of MnO as shown in Fig. 1(a). This demonstrated a clear difference of Mn species

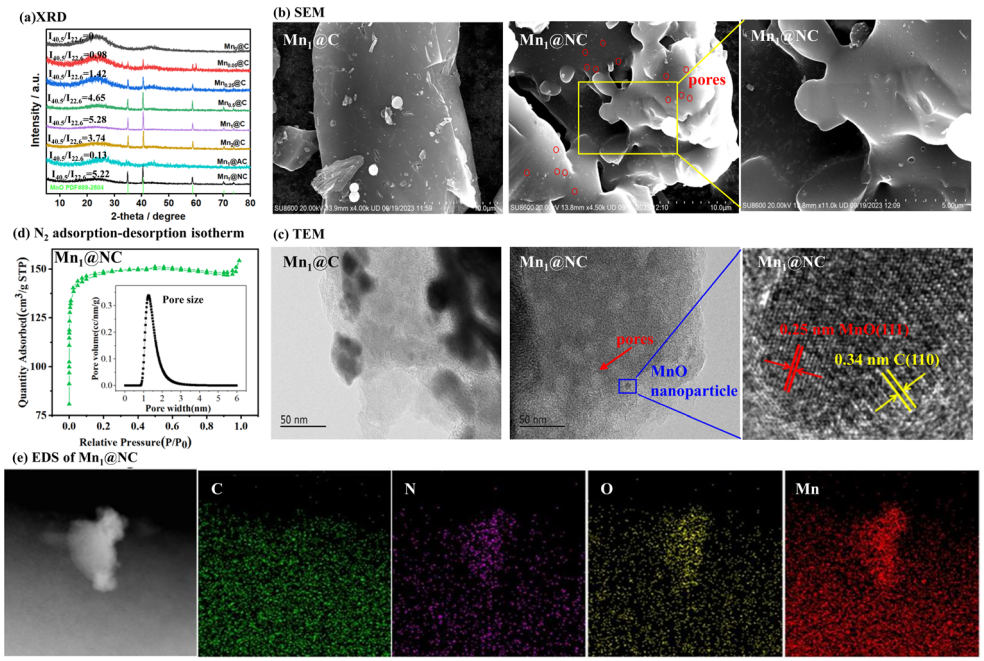

Fig. 1 XRD spectra (a), SEM images (b), TEM images (c), N_2 adsorption–desorption curves (d) and elemental mapping (e) of Mn_x@C and Mn_1@NC.

between the Mn_x@C prepared *in situ* from lignin and Mn_1@AC prepared *via* the conventional method (*i.e.*, impregnation method).

Fig. 1(b) shows the SEM images of Mn_1@C and Mn_1@NC. In the absence of NH_4Cl, Mn_1@C exhibited a bulk morphology with obvious agglomeration of Mn species. The addition of NH_4Cl significantly altered the morphology of Mn_1@NC, transforming from a bulk structure of Mn_1@C to a porous lamellar structure of Mn_1@NC. Fig. 1(b) also shows a substantial population of pores in Mn_1@NC, partially labelled with red circles. Fig. 1(c) shows the TEM images of Mn_1@C and Mn_1@NC. Obviously, a large number of pores were observed in Mn_1@NC with 7–10 nm of nanoparticles, while Mn_1@C possessed large nanoparticles without pores observed. Fig. 1(c) also illustrates the MnO nanocrystals that are surrounded by amorphous carbon or graphene. The lattice fringe with a spacing of 0.25 nm corresponded to the (111) plane of the cubic MnO phase, and a spacing of 0.34 nm corresponded to the highly organized crystal carbon structure, which was thought to be the graphene layer. These results were consistent with the XRD results, as shown in Fig. 1(a). Fig. 1(d) shows the N_2 adsorption–desorption isotherm of Mn_1@NC. N_2 adsorption–desorption test did not provide the isotherm of Mn_1@C, which indicated that Mn_1@C was a non-porous material. Mn_1@NC exhibited a typical type I isotherm, indicating that Mn_1@NC was microporous with abundant micropores. The surface area of Mn_1@NC was 567.0 $m^2\ g^{-1}$ and the micropore area was 549.8 $m^2\ g^{-1}$, while the pore diameter in Mn_1@NC as shown in Fig. 1(d) was 1.26 nm. As mentioned above, volatiles from lignin decomposition, NH_3 and HCl from NH_4Cl were formed during the co-carbonization of NH_4Cl and the Mn–lignin complex. The evolution of these gases (volatiles, NH_3 and HCl) promoted the pore formation in carbon materials. At the same time, NH_3 and HCl reacted with carbon-based intermediates or active groups to achieve morphology regulation through a complex synergistic effect.[39,40] For example, the released HCl acted as an acid catalyst to break the C–C or C–O bonds and to promote the formation of condensed ring structures during lignin carbonization.[41] With the increase in temperature, lignin decomposed extensively to produce small-molecule gases (*e.g.*, CO_2, H_2O). The continuous escape of these gases generated pores and constructed an interconnected porous network.[41,42] Fig. 1(e) shows the elemental mapping of carbon (C), nitrogen (N), oxygen (O) and Mn in Mn_1@NC. As shown in Fig. 1(e), there was a certain correlation between the distributions of O and Mn, which corresponds to the formation of MnO. N was doped in the prepared Mn_1@NC, exhibiting a distribution similar to that of O and Mn.

OER performance

Fig. 2(a) shows the LSV curves for the OER of Mn_x@C prepared at different Mn proportions. The overpotentials (E_{50}) of Mn_x@C at a current density of 50 mA cm^{-2} for the OER are illustrated in Fig. 2(b). Fig. 2(a) and (b) indicate that the OER performance of Mn_x@C was affected by the Mn proportion. The LSV curves of Mn_x@C shifted to a low potential zone with the Mn proportion increasing to 1 mmol g^{-1}. The E_{50} decreased from 618 mV to 517 mV with the Mn proportion increasing to 1 mmol g^{-1}. When the proportion of Mn was 1 mmol g^{-1}, Mn_1@C exhibited

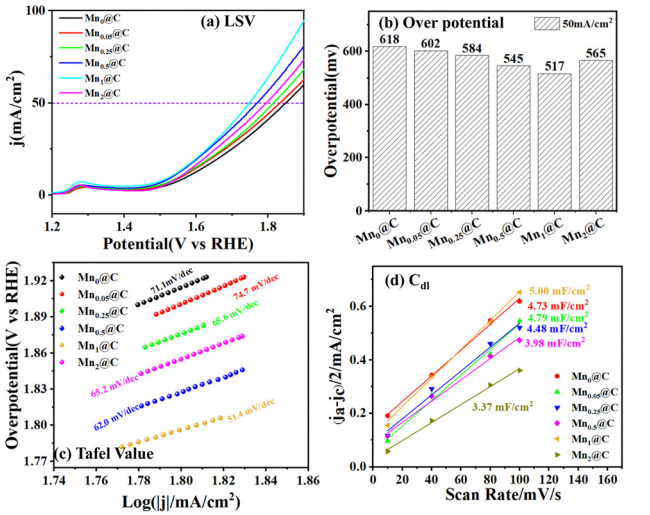

Fig. 2 The effects of Mn proportion on the OER performance of electrode material Mn_x@C. (a) LSV; (b) overpotential at 50 mA cm^{-2}; (c) Tafel value; (d) C_{dl}.

the best OER catalytic performance with the lowest E_{50} of 517 mV. Further increase with the Mn proportion led to the decrease of OER performance with a higher E_{50} of 565 mV at 2 mmol g^{-1} than that at 1 mmol g^{-1}. Fig. 2(c) shows the Tafel slopes of Mn_x@C corresponding to the LSV curves for the OER. Except Mn_1@C, the Tafel slopes of Mn_x@C were above 60 mV dec^{-1}, indicating that the rate-determining step (RDS) of the OER was dominated by a single-electron transfer step for the formation of the oxygen intermediate (*O) and the peroxide intermediate (*OOH). Mn_1@C exhibited the lowest Tafel slope (51.4 mV dec^{-1}), indicating that Mn_1@C exhibited the fastest OER kinetic process among all the *in situ* prepared catalysts. The Tafel slope of Mn_1@C was slightly lower than the theoretical value (60 mV dec^{-1}), indicating that it was still dominated by a single-electron transfer as RDS, accompanied by a slight synergistic effect of multi-step reactions. Fig. 2(d) illustrates that the double-layer capacitance (C_{dl}) of Mn_1@C was higher than that of other Mn_x@C, indicating that the electrochemical active area of Mn_1@C was larger than other Mn_x@C. Above all, Mn_1@C exhibited the best OER catalytic performance.

Comparing the OER performance of Mn_1@C and Mn_1@AC in Fig. 3, the OER performance of Mn_1@C was significantly poorer than that of Mn_1@AC prepared with AC as the support. As shown in Fig. 3(b), the E_{50} of Mn_1@AC was 434 mV, lower than that of Mn_1@C (517 mV). Fig. 3(c) shows that the Tafel slope of Mn_1@AC was 53.9 mV dec^{-1}, slightly higher than that of Mn_1@C, indicating that Mn_1@AC had a slower OER kinetic process than Mn_1@C. As illustrated in Fig. 3(d), the C_{dl} of Mn_1@AC (5.40 mF cm^{-2}) was higher than that of Mn_1@C (5.00 mF cm^{-2}), indicating that the electrochemical active area of Mn_1@AC was higher than that of Mn_1@C. The higher electrochemical active area of Mn_1@AC was possibly due to the fact that AC has abundant pores, which facilitated substrate adsorption and electron transmission, thereby improving the OER performance.

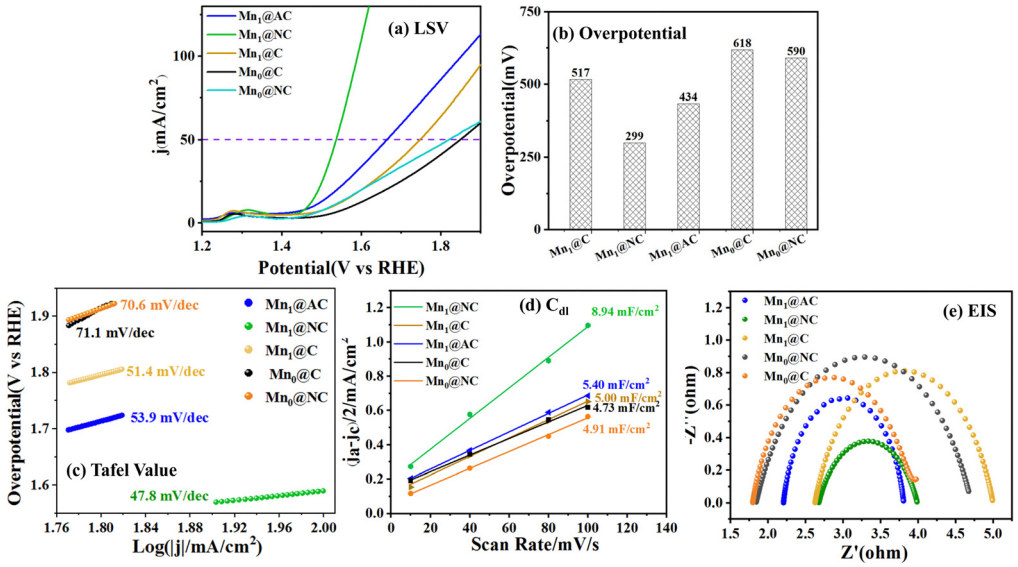

Fig. 3 NH_4Cl effect on the OER performance of electrode materials Mn_1@C and Mn_1@NC. (a) LSV; (b) overpotential at 50 mA cm^{-2}; (c) Tafel value; (d) C_{dl}; (e) EIS.

To optimize the pore structure of Mn_1@C prepared by *in situ* carbonization of lignin, NH_4Cl was added as a pore-forming agent into the Mn-chelated lignin samples. As discussed in Section 2.1, with the addition of NH_4Cl, Mn_1@NC had more developed pore structures and higher specific surface area than Mn_1@C. Fig. 3(a) and (b) show that the E_{50} decreased from 517 mV for Mn_1@C to 299 mV for Mn_1@NC, which was much lower than that of Mn_1@AC (434 mV). Fig. 3(c) shows the Tafel slope of Mn_1@NC (47.8 mV dec^{-1}) was much lower than that of Mn_1@C (51.4 mV dec^{-1}) and Mn_1@AC (53.9 mV dec^{-1}), indicating that Mn_1@NC had a faster OER kinetic process than Mn_1@C and Mn_1@AC. As shown in Fig. 3(d), the C_{dl} of Mn_1@NC reached 8.94 mF cm^{-2}, which was much higher than that of Mn_1@C (5.38 mF cm^{-2}) and Mn_1@AC (5.40 mF cm^{-2}), indicating that the addition of NH_4Cl effectively increased the electrochemical active area of the Mn-doped lignin carbon material. Fig. 3(e) illustrates that the charge transfer resistances (R_{ct}) increased in the order of Mn_1@NC < Mn_1@AC< Mn_1@C, indicating that Mn_1@NC had the fastest charge transfer rate during the catalytic OER process. Above all, the addition of NH_4Cl significantly improved the OER performance of Mn_1@NC, due to the adjusted pore structures and high specific surface area.

As shown in Fig. 3, the NH_4Cl-added carbon material (Mn_0@NC) without Mn-loading was also studied to further illustrate the effects of Mn-loading and NH_4Cl-addition on the OER performance. The OER performance of Mn_0@NC was slightly enhanced with a lower E_{50} (590 mV), a smaller Tafel slope (70.6 mV dec^{-1}), and a higher C_{dl} (4.91 mF cm^{-2}) than Mn_0@C, indicating that NH_4Cl-addition was beneficial for the improvement of OER performance, possibly due to the regulated morphology and N-doping. Comparing the NH_4Cl-free materials (Mn_1@C) and Mn-free materials (Mn_0@NC) with Mn and N co-doped materials (Mn_1@NC), the much better OER performances of Mn_1@NC indicated that Mn-loading and NH_4Cl-addition played a crucial synergistic role in enhancing the OER performance.

Fig. 4 summarizes the OER overpotential (E_{10}) at 10 mA cm^{-2} of Mn_1@NC and the reported Mn-based catalysts.[18,19,28,30,43] As illustrated in Fig. 4, Mn_1@NC, prepared *via* an *in situ* anchoring and direct carbonization strategy in this work, has a much lower E_{10} (235 mV) than the reported Mn-based catalysts. In other words, Mn_1@NC exhibited more excellent OER catalytic activity than the reported Mn-based catalysts. The *in situ* anchoring and direct carbonization strategy using lignin as the carbon source provided a simple, cost-effective, and scalable route to high-performance Mn-based catalysts from lignin, offering significant potential for industrial water electrolysis.

HER performance

Fig. 5(a) shows the LSV curves for the HER of Mn_x@C prepared with different Mn proportions. The Mn proportion obviously affected the HER performance of Mn_x@C. The LSV curves for the

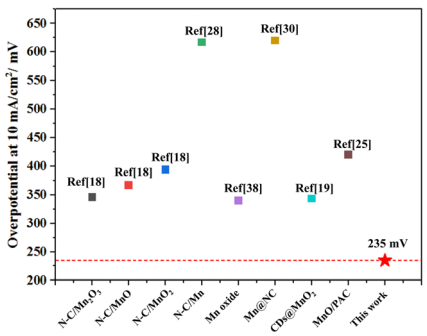

Fig. 4 The overpotential of Mn_1@NC at 10 mA cm^{-2} compared with the reported Mn-based catalysts.

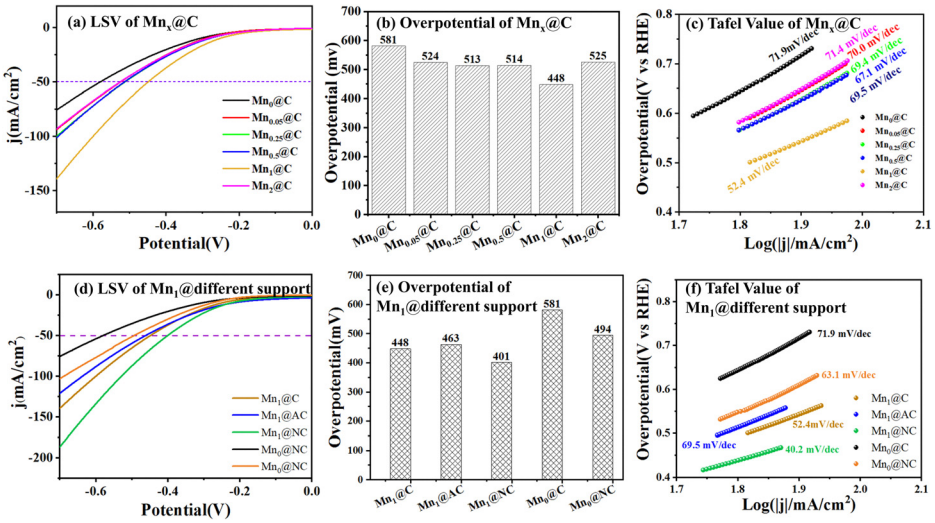

Fig. 5 The effects of Mn proportion (a)–(c) on the HER performance of electrode material Mn$_x$@C, and NH_4Cl effect (d)–(f) on the HER performance of electrode materials Mn$_1$@C and Mn$_1$@NC.

HER shifted to a lower potential zone with the Mn proportion increasing to 1 mmol g^{-1} as shown in Fig. 5(a). Fig. 5(b) illustrates the E_{50} of Mn$_x$@C at a current density of 50 mA cm^{-2} for the HER. The E_{50} decreased from 581 mV to 448 mV with the Mn proportion increasing to 1 mmol g^{-1}. When the Mn proportion was 1 mmol g^{-1}, Mn$_1$@C had the lowest E_{50} of 448 mV, showing the best HER performance. However, the LSV curve for the HER of Mn$_2$@C shifted to a higher potential zone at the Mn proportion of 2 mmol g^{-1}, as shown in Fig. 5(a), and the E_{50} of Mn$_2$@C increased to 525 mV, as shown in Fig. 5(b), which indicated that a high Mn proportion of 2 mmol g^{-1} led to a decreased HER performance of Mn$_2$@C. Fig. 5(c) illustrates the Tafel slope of Mn$_x$@C. All the Tafel slopes were between 40 mV dec^{-1} and 20 mV dec^{-1}, indicating that the control step was the Heyrovsky reaction in the Volmer–Heyrovsky mechanism (electrochemical desorption mechanism).[44–46] As shown in Fig. 5(c), Mn$_1$@C had the smallest Tafel slope (52.4 mV dec^{-1}) among all the prepared catalysts, indicating that Mn$_1$@C exhibited the fastest kinetic process of the HER, and the most excellent catalytic activity for the HER.

Fig. 5(d–f) shows the HER performance of Mn$_1$@C, Mn$_1$@AC and Mn$_1$@NC. Compared with the Mn$_1$@AC prepared *via* the conventional method, Mn$_1$@C exhibited a lower E_{50} (448 mV) than Mn$_1$@AC (525 mV) as illustrated in Fig. 5(e), indicating that lignin-derived *in situ* prepared Mn$_1$@C achieved higher HER performance than Mn$_1$@AC synthesized by the conventional method (*i.e.*, the impregnation method). Similarly with the OER performance, NH_4Cl-added and Mn-free carbon materials (Mn$_0$@NC) also exhibited a better HER performance than Mn$_0$@C, as evidenced by a lower E_{50} (494 mV). Additionally, Mn$_0$@NC outperformed Mn$_0$@C, and Mn$_1$@NC outperformed Mn$_1$@C in HER performance, indicating that the NH_4Cl-addition played important roles in improving HER activity. The synergistic effect of the Mn-loading and NH_4Cl-addition endowed Mn$_1$@NC with the optimal HER performance. As shown in Fig. 5(d), the LSV curve of Mn$_1$@NC shifted to a lower potential zone than that of Mn$_1$@C. Fig. 5(e) further reveals that Mn$_1$@NC had a lower E_{50} (409 mV) than Mn$_1$@C (448 mV), demonstrating that NH_4Cl-addition obviously lowered the overpotential and improved the HER performance of Mn-loaded carbon materials. Furthermore, Fig. 5(f) shows that the Tafel slope of Mn$_1$@NC (40.2 mV dec^{-1}) was remarkably lower than that of Mn$_1$@C (52.4 mV dec^{-1}), indicating that NH_4Cl-addition promoted the Heyrovsky reaction during the HER and accelerated the reaction kinetics. As previously discussed, the decomposition of NH_4Cl during the preparation of Mn$_1$@NC generated abundant pores and a high specific surface area, which facilitated proton transfer and thereby improved the HER performance.

Stability test and the overall water splitting

Fig. 6(a) shows the stability of Mn$_1$@C and Mn$_1$@NC at a constant voltage. Both Mn$_1$@C and Mn$_1$@NC exhibited a trend of current decline during the initial testing stage, mainly due to the change in the chemical valence of Mn in Mn$_1$@C and Mn$_1$@NC during the initial power-on process. As the test progressed, the current of Mn$_1$@C and Mn$_1$@NC stabilized at a current retention rate of 94% and 96% following a 24 h stability assessment, respectively, indicating that both Mn$_1$@C and Mn$_1$@NC had good stability. As mentioned earlier, the polar functional groups in the lignin structure can form coordination bonds with Mn and stabilize Mn anchored in the carbon-based support, thereby avoiding the loss of Mn during application. Additionally, the doping of N enhanced the anchoring effect of the carbon-based support on the metal. Hence, Mn$_1$@NC exhibited greater stability than Mn$_1$@C. The LSV curves of Mn$_1$@C and Mn$_1$@NC after the stability test were also tested and are shown in Fig. 6(a). The LSV curve of Mn$_1$@C-tested slightly shifted to a higher potential zone than Mn$_1$@C as prepared, while the LSV curve of Mn$_1$@NC C-tested was almost the same as for Mn$_1$@NC as prepared. This result indicated the good stability of Mn$_1$@NC and the N-doping enhanced the stability.

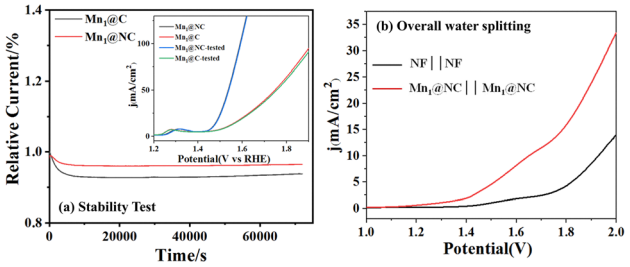

Fig. 6 (a) Stability test of Mn_1@C and Mn_1@NC; (b) LSV curves for overall water splitting using Mn_1@NC‖Mn_1@NC.

Encouraged by the extraordinary activity of Mn_1@NC for the HER and the OER in alkaline media, a two-electrode system was assembled in a 1.0 M KOH solution with Mn_1@NC serving as both the cathode and anode (Mn_1@NC‖Mn_1@NC). The LSV curves for overall water splitting using Mn_1@NC‖Mn_1@NC are shown in Fig. 6(b). The device afforded the current densities of 10 mA cm^{-2} at cell voltages of 1.65 V, which outperforms NF‖NF (1.946 V).

The formation process of Mn_1@NC and the real active site

Fig. 7 shows the XPS spectra of C 1s, O 1s, Mn 2p, and N 1s of Mn_1@NC before test (a–d) and after test (e–h). The high-resolution XPS spectrum of C 1s was deconvoluted into three peaks at 284.8 eV, 286.1 eV, and 288.9 eV, corresponding to C–C (sp^2 carbon), C–O–C (ether/alkoxy groups), and O–C═O (carboxyl/ester groups), respectively. More O–C═O was detected on the surface of Mn_1@NC after the test. Another two peaks observed in Fig. 7(e) were caused by the K adsorbed on the surface of Mn_1@NC during the OER test. Three deconvoluted peaks at 531 eV, 532 eV and 533 eV, as shown in Fig. 7(b and f), were assigned to Mn–O, Mn–O–C, and C═O. There was a new deconvoluted peak assigned to defect O at 529.8 eV, as shown in Fig. 7(f), which was beneficial for the OER.[47,48] The high-resolution XPS spectrum of Mn $2p_{1/2}$ in Fig. 7(c and g) was at 653.6 eV. The high-resolution XPS spectra of Mn $2p_{3/2}$ in Fig. 7(c) were well deconvoluted into five peaks at 638.1 eV, 641.1 eV, 642.8 eV, 644.6 eV and 646.9 eV, which were assigned to Mn^0, MnO, Mn_2O_3, MnO_2, and MnO.[49,50] Mn exhibited multiple chemical oxidation states on the surface of Mn_1@NC before the test. Obviously, Mn $2p_{3/2}$ of Mn_1@NC after the stability test, as shown in Fig. 7(g), was mainly MnOOH, which worked as the real active site for the OER.[20] Mn^0 and MnO were oxidized to MnOOH. The N content on the surface of Mn_1@NC reduced from 3.47 wt% (before test) to 1.52 wt% after the test, resulting from the N leaching out during the OER process. The N on the surface of Mn_1@NC existed as graphitic N (401.1 eV), pyridinic N (399.8 eV) and pyrrolic N (398.8 eV) as assigned in Fig. 7(d and h).[51] Among these N species, graphitic N was the main N component on the surface of Mn_1@NC due to its higher area proportion. The graphitic N was reported to promote the electron transport with high electron-transfer capacity.[51,52] The pyridinic N and pyrrolic N brought heteroatomic doping defects on the surface of Mn_1@NC.[53] The relative area proportion of pyrrolic N decreased, while the relative area proportion of pyridinic N increased, indicating that pyridinic N was more stable than pyrrolic N during the OER process.

Above all, the formation process of Mn_1@NC and the real active site for the OER process can be summarized as follows. First, Mn^{2+} underwent self-assembly with lignin due to the chelation–anchoring interaction between the polar oxygen-containing functional groups of lignin and Mn^{2+}. The chelation–anchoring interaction permitted Mn^{2+} to be well dispersed in lignin carbon. Secondly, carbothermal reduction occurred, generating Mn^0 during the *in situ* carbonization process. Simultaneously, due to the complex and highly reactive nature of lignin depolymerization products, redox reactions took place with Mn^0 or Mn^{2+}, forming Mn_2O_3, MnO_2, or MnO. Among these MnO_x species, MnO was the main MnO_x species, and its aggregation

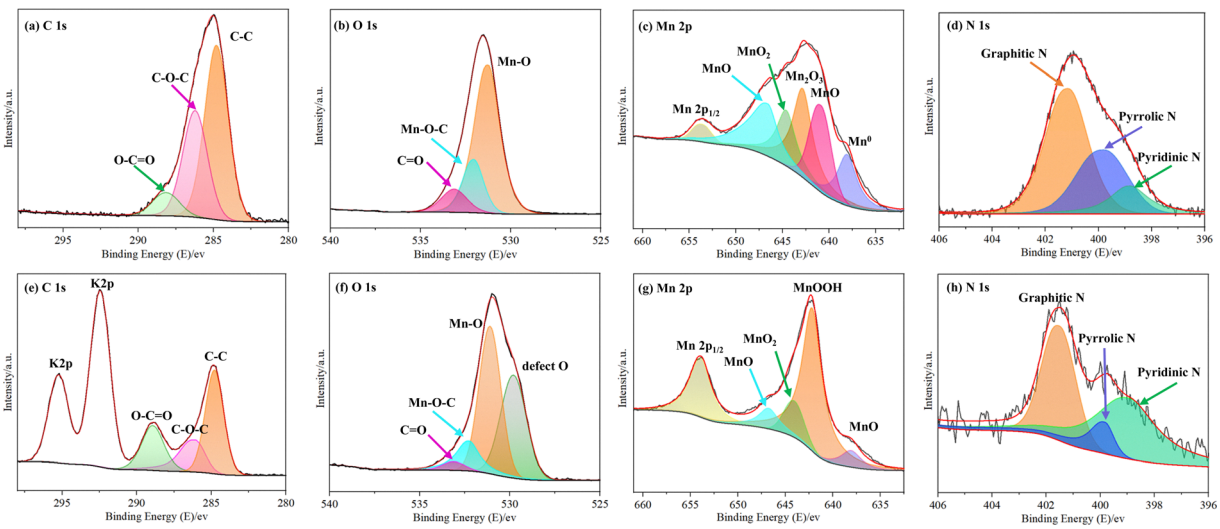

Fig. 7 XPS spectra of (a) and (e) C 1s, (b) and (f) O 1s, (c) and (g) Mn 2p, and (d) and (h) N 1s of Mn_1@NC before the stability test (a)–(d) and after the stability test (e)–(h).

nanoparticles dispersed in the lignin-based carbon support, while Mn_2O_3, MnO_2, and Mn^0 were primarily dispersed in an amorphous state on the Mn_1@NC surface. NH_4Cl was decomposed into HCl and NH_3 during the co-carbonization of NH_4Cl with Mn–lignin.[24] The outgassing of HCl and NH_3 acted as a pore-forming agent, regulating the carbonization process of the lignin-derived carbon, which resulted in the formation of a sheet-like porous carbon structure while concurrently achieving N-doped carbon. During the initial stage of the OER, the low-valent manganese species (Mn^0 and MnO) in Mn_1@NC underwent oxidation to Mn species with +3 valence. MnO_2, as a common precursor of Mn-based OER catalysts, underwent reduction–reconstruction reactions to form Mn species with +3 valence in the OER test. The formed Mn species with +3 valence then combined with the hydroxide anion (OH^-) in KOH solution to form a stable structure of MnOOH through proton transfer and coordination structure adjustment during the OER test. MnOOH was the real active species. OH^- in KOH was first adsorbed on the Mn site of MnOOH forming adsorbed Mn^{3+}–OH intermediates. Then, Mn^{3+}–OH intermediates were oxidized to form Mn^{4+}–O substances with the loss of one electron (e^-) and one proton (H^+). Two adjacent Mn^{4+}–O intermediates underwent O–O bond coupling to form the Mn–O–O–Mn peroxide intermediate, which continued to undergo an oxidation reaction, losing electrons and adjusting its coordination structure. Finally, the Mn–O bond broke to release O_2 molecules. Meanwhile, the Mn active sites were reduced to the initial +3 valence state, recombining with OH^- in the electrolyte to enter the next catalytic cycle.[20]

Conclusions

This study successfully fabricated Mn-loaded lignin-derived carbon catalysts *via* an *in situ* anchoring and one-step carbonization strategy. Characterization studies confirmed that the *in situ* process enabled effective incorporation and uniform dispersion of Mn species (mainly MnO, Mn_2O_3, and MnO_2), where MnO existed as aggregated nanoparticles and Mn_2O_3/MnO_2 as amorphous phases. The Mn proportion had a significant impact on catalytic performance: the optimal Mn proportion was 1 mmol g^{-1} lignin, and Mn_1@C exhibited the best OER and HER activity among Mn_x@C samples, and had the lowest overpotential of 517 mV (OER) and 448 mV (HER) at 50 mA cm^{-2}. Notably, NH_4Cl modification played a dual role—serving as a pore-forming agent to construct a layered microporous structure (enhancing specific surface area and active site exposure) and a nitrogen source to realize N-doping (improving charge transfer efficiency). This modification enhanced the OER and HER activity of Mn_1@NC, 299 mV (OER) and 409 mV (HER) at 50 mA cm^{-2}, which outperformed both Mn_1@C and Mn_1@AC prepared by the conventional method. The comparison among OER performances of Mn_1@NC, Mn_1@C, Mn_0@NC and Mn_0@C indicated that the Mn-loading and NH_4Cl-addition played a crucial synergistic role in enhancing the OER and HER performances for water electrolysis. Furthermore, Mn_1@NC showed excellent long-term stability and enabled overall water-splitting to reach 10 mA cm^{-2} at 1.65 V using Mn_1@NC‖Mn_1@NC. This study simplified the preparation process of metal-loaded carbon-based electrode materials and provided a reference for the preparation and application of biomass carbon-based composite materials.

Author contributions

Conceptualization: H. Y. and C. L.; methodology: H. Y. and C. L.; validation: M. Y., H. Y. and B. W.; formal analysis: B. W., H. Y. and M. Y.; data curation: M. Y., H. Y. and B. W.; writing – original draft preparation: H. Y.; writing – review and editing: H. Y. and C. L.; visualization: H. Y.; supervision: H. Y. and C. L.; funding acquisition: C. L. All authors have read and agreed to the published version of the manuscript.

Conflicts of interest

There are no conflicts of interest to declare.

Data availability

The experiments, observations and data that support the findings of this study are included in this manuscript.

Acknowledgements

This work was supported by the National Key R&D Program of China (2023YFA1507902), and the National Natural Science Foundation of China (U25A20332).

References

1 M. Liu, Z. Yao, J. Gu, C. Li, X. Huang, L. Zhang, Z. Huang and M. Fan, *Chem. Eng. J.*, 2023, **461**, 141918.
2 H. Yang, Z. Chen, K. Luo, M. Yu and Y. Zhang, *New J. Chem.*, 2024, **48**, 8690–8701.
3 K. Qin, H. Yu, W. Zhu, Y. Zhou, Z. Guo, Q. Shao, Y. Wu, X. Wang, Y. Li, Y. Ji, F. Liao, Y. Liu, Z. Kang and M. Shao, *Adv. Funct. Mater.*, 2025, **35**, 2402226.
4 P. Salimi and M. M. Najafpour, *Chem. – Eur. J.*, 2020, **26**, 17063–17068.
5 S. Madadkhani, S. I. Allakhverdiev and M. M. Najafpour, *New J. Chem.*, 2020, **44**, 15636–15645.
6 M. S. A. Akbari, S. Nandy, K. H. Chae, P. Aleshkevych and M. M. Najafpour, *ACS Appl. Energy Mater.*, 2024, **7**, 3299–3308.
7 W. Zhang, M. Liu, X. Gu, Y. Shi, Z. Deng and N. Cai, *Chem. Rev.*, 2023, **123**, 7119–7192.
8 Y. Feng, H. Yang, X. Wang, C. Hu, H. Jing and J. Cheng, *Int. J. Hydrogen Energy*, 2022, **47**, 17946–17970.
9 H. Wang, K. H. L. Zhang, J. P. Hofmann, V. A. Pena OShea and F. E. Oropeza, *J. Mater. Chem. A*, 2021, **9**, 19465–19488.
10 X. Qiao, X. Yin, L. Wen, X. Chen, J. Li, H. Ye, X. Huang, W. Zhao and T. Wang, *Chem*, 2022, **8**, 3241–3251.

11 M. Farajzadeh and F. R. Rahsepar, *ChemElectroChem*, 2024, **11**, e202300516.
12 X. Huo, H. Yu, B. Xing, X. Zuo and N. Zhang, *Chem. Rec.*, 2022, **22**, e202200175.
13 X. Song, C. Fan, Y. Tang, Y. Ren, Z. Zang, L. Li, X. Yu, Z. Lu, X. Yang and X. Zhang, *Fuel*, 2025, **381**, 133558.
14 M. Gharedaghloo and M. M. Najafpour, *ACS Appl. Energy Mater.*, 2024, **7**, 10081–10091.
15 M. Huynh, C. Shi, S. J. L. Billinge and D. G. Nocera, *J. Am. Chem. Soc.*, 2015, **137**, 14887–14904.
16 H. Tian, L. Zeng, Y. Huang, Z. Ma, G. Meng, L. Peng, C. Chen, X. Cui and J. Shi, *Nano-Micro Lett.*, 2020, **12**, 161.
17 Y. Wang, Y. Zhang, G. Gao, Y. Fan, R. Wang, J. Feng, L. Yang, A. Meng, J. Zhao and Z. Li, *Nano-Micro Lett.*, 2023, **15**, 219.
18 X. Zhai, X. Wang, X. Pang, J. Zhang, Q. Wu, W. Na, Y. Zhou and L. Tian, *J. Taiwan Inst. Chem. Eng.*, 2021, **126**, 383–391.
19 Y. Zhang, Z. Liu, F. Guo, M. Li and X. Bo, *J. Colloid Interface Sci.*, 2022, **618**, 149–160.
20 P. Wang, S. Zhang, Z. Wang, Y. Mo, X. Luo, F. Yang, M. Lv, Z. Li and X. Liu, *J. Mater. Chem. A*, 2023, **11**, 5476–5494.
21 L. Tian, X. Zhai, X. Wang, J. Li and Z. Li, *J. Mater. Chem. A*, 2020, **8**, 14400–14414.
22 Y. Hu, B. Shen, W. Liu, Y. Pan, J. Huang, X. Zhu, Z. Guo, Y. Xiao, J. Cheng and J. Qu, *J. Alloys Compd.*, 2025, **1010**, 178251.
23 G. Zhang, B. Hu, Y. Luo, Y. Xie, Y. Chen, Y. Zhang, Y. Ling, J. Zou and Y. Shao, *Int. J. Hydrogen Energy*, 2024, **53**, 1226–1232.
24 A. Muzammil, R. Haider, W. Wei, L. Li, L. Wu, Y. Fan and X. Yuan, *ACS Appl. Mater. Interfaces*, 2025, **17**, 22812–22821.
25 X. F. Lu, Y. Chen, S. Wang, S. Gao and X. W. Lou, *Adv. Mater.*, 2019, **31**, 1902339.
26 S. Chandrasekaran, E. Arumugam, S. Ramasamy, C. Karuppiah, S. Bhaskaran, C. C. Yang, D. Nallapandi and K. Palanisamy, *Int. J. Hydrogen Energy*, 2023, **48**, 10423–10437.
27 J. Liu, J. Zhang, H. Zhou, B. Liu, H. Dong, X. Lin and Y. Qin, *J. Colloid Interface Sci.*, 2023, **629**, 822–831.
28 L. Tian, J. Wang, K. Wang, H. Wo, X. Wang, W. Zhuang, T. Li and X. Du, *Carbon*, 2019, **143**, 457–466.
29 S. Sangeetha, G. Krishnamurthy, S. Foro and K. Raj, *J. Inorg. Organomet. Polym*, 2020, **30**, 4792–4802.
30 N. Zhang, P. Cui, J. Zhang and Y. Qiao, *Catalysts*, 2025, **15**, 579.
31 W. Li, G. Wang, W. Zhang, J. Li, B. Zhang and C. Si, *Ind. Crops Prod.*, 2023, **204**, 117342.
32 K. L. A. Cao, Y. Kitamoto, F. Iskandar and T. Ogi, *Adv. Powder Technol.*, 2021, **32**, 2064–2073.
33 F. Chen, W. Zhou, H. Yao, P. Fan, J. Yang, Z. Fei and M. Zhong, *Green Chem.*, 2013, **15**, 3057–3063.
34 Z. Chen, H. Lai, H. Zhuo, Y. L. Zhong, L. Zhong and X. Peng, *Collagen Leather*, 2023, **5**, 15.
35 Z. Cheng, Z. Li, S. Huang, J. Pan, J. Mei, S. Zhang, X. Peng, W. Lu and L. Yan, *Catalysts*, 2025, **15**, 503.
36 T. Li, B. Chen, M. Cao, X. Ouyang, X. Qiu and C. Li, *AIChE J.*, 2023, **69**, e17877.
37 W. Zhang, J. Yin, C. Wang, L. Zhao, W. Jian, K. Lu, H. Lin, X. Qiu and H. N. Alshareef, *Small Methods*, 2021, **5**, 2100896.
38 H. M. Yang, S. Apparia, S. Kudo, J.-I. Hayash and K. Norinaga, *Ind. Eng. Chem. Res.*, 2015, **54**(27), 6855–6864.
39 W. Chen, Y. Chen, H. Yang, K. Li, X. Chen and H. Chen, *Bioresour. Technol.*, 2018, **249**, 247–253.
40 W. Chen, K. Li, M. Xia, Y. Chen, H. Yang, C. Zhiquan, X. Chen and H. Chen, *Bioresour. Technol.*, 2018, **263**, 350–357.
41 Z. Wu, L. Hu, Y. Jiang, X. Wang, J. Xu, Q. Wang and S. Jiang, *Biomass Convers. Biorefin.*, 2023, **13**, 519–539.
42 Y. Chen, Y. Jiang, D. Tian, J. Hu, J. He, G. Yang, L. Luo, Y. Xiao, S. Deng, O. Deng, W. Zhou and F. Shen, *Int. J. Biol. Macromol.*, 2020, **164**, 3038–3047.
43 Y. Gorlin and T. F. Jaramillo, *J. Am. Chem. Soc.*, 2010, **132**, 13612–13614.
44 J. Wang, W. Zang, X. Liu, J. Sun, S. Xi, W. Liu, Z. Kou, L. Shen and J. Wang, *Small*, 2024, **20**, 2309427.
45 F. Bao, E. Kemppainen, I. Dorbandt, R. Bors, F. Xi, R. Schlatmann, R. van de Krol and S. Calnan, *ChemElectroChem*, 2021, **8**, 195–208.
46 C. Wan, Y. Ling, S. Wang, H. Pu, Y. Huang and X. Duan, *ACS Cent. Sci.*, 2024, **10**, 658–665.
47 Y. Wu, C. Guo, R. Yao, K. Zhang, J. Li and G. Liu, *Adv. Funct. Mater.*, 2024, **34**, 2410193.
48 X. Chen, R. Ma, W. Jia, X. Cao, J. Zhang, F. Cheng and L. Jiao, *Chem Catal.*, 2025, **5**, 101335.
49 M. C. Biesinger, B. P. Payne, A. P. Grosvenor, L. W. M. Lau, A. R. Gerson and R. S. C. Smart, *Appl. Surf. Sci.*, 2011, **257**, 2717–2730.
50 E. S. Ilton, J. E. Post, P. J. Heaney, F. T. Ling and S. N. Kerisit, *Appl. Surf. Sci.*, 2016, **366**, 475–485.
51 G. Qu, P. Jia, S. Tang, M. N. Pervez, Y. Pang, B. Li, C. Cao and Y. Zhao, *J. Hazard. Mater.*, 2024, **461**, 132626.
52 T. Marshall-Roth, N. J. Libretto, A. T. Wrobel, K. J. Anderton, M. L. Pegis, N. D. Ricke, T. V. Voorhis, J. T. Miller and Y. Surendranath, *Nat. Commun.*, 2020, **11**, 5283.
53 M. Liu, M. Liu, W. Chen, F. Li, S. Cai, S. J. Lin, X. Chen and Z. Cai, *Angew. Chem., Int. Ed.*, 2025, **64**, e202421755.

